

pubs.acs.org/JPCC Article

# Data-Intensive Exploration of the Photoelectrochemical Responses of Main-Group Metal Sulfides

Rowan R. Katzbaer, Simon Gelin, Monica J. Theibault, Mohammed M. Khan, Cierra Chandler, Nicola Colonna, Zhiqiang Mao, Héctor D. Abruña,\* Ismaila Dabo,\* and Raymond E. Schaak\*



Cite This: J. Phys. Chem. C 2024, 128, 8874-8882



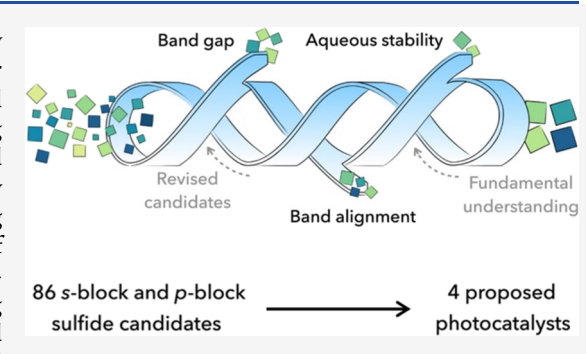
**ACCESS** I

III Metrics & More

Article Recommendations

s Supporting Information

**ABSTRACT:** Materials that efficiently promote the thermodynamically uphill water-splitting reaction under solar illumination are essential for generating carbon-free ("green") hydrogen. Mapping out the combinatorial space of potential photocatalysts for this reaction can be expedited using data-intensive materials exploration. The calculated band gaps and band alignments can serve as key indicators and metrics to computationally screen photoactive materials. Ternary main-group metal sulfides containing *p*- and *s*-block elements represent a promising, albeit underexplored, class of photocatalysts. Here, we computationally screen 86 candidate ternary maingroup metal sulfides containing *p*- and *s*-block elements. By validating electronic structure predictions against experimental band gaps and band edges for synthetically accessible materials, we propose eight potential



photocatalysts. Using computed Pourbaix diagrams, we further narrowed the candidate pool to four materials based on the predicted aqueous stability. We then synthesized and characterized these four materials and experimentally screened them for photoresponsiveness under photocatalytically relevant conditions. We also characterized their experimental band gaps and band edge positions and compared them with computational predictions. Based on the experimental screening protocols, we identify MgIn<sub>2</sub>S<sub>4</sub> and BaSn<sub>2</sub>S<sub>5</sub> as photoresponsive materials with sufficient aqueous stability to be considered in greater depth as potential photocatalysts for overall water-splitting.

# INTRODUCTION

Materials discovery can be limited in both bandwidth and scope by synthetic constraints. Making and experimentally validating candidate materials that have complex compositions and structures, which generally offer the greatest functional tunability, must often be done serially, making rapid screening impractical. Additionally, synthesis becomes more challenging for such complex materials, as the number of possible byproducts increases, as well as the occurrence of impurities that may strongly affect performance. In response to this challenge, the rational, application-focused design of materials can be accelerated using data-intensive approaches, where computational screening helps narrow the scope of candidate materials to a synthetically tractable number of compositional and structural options.

In the field of energy conversion and storage, circumventing the synthetic bottleneck to speed up materials discovery is especially important and challenging. As the detrimental effects of climate change become increasingly frequent and severe, the identification of high-performing photocatalysts for overall water splitting could provide a pathway to deep decarbonization by enabling sunlight and water to generate "green" hydrogen as a fuel that would, in turn, replace the burning of fossil fuels. <sup>1–3</sup> Photocatalysts are amenable to high-throughput

screening as their performance can be effectively estimated by examining their band structures and the energies of their valence and conduction band edges (i.e., band alignment), which are foundational criteria for assessing the feasibility of photocatalytic overall water splitting. While this approach does not account for interfacial processes, which are much more computationally demanding to model but are an integral part of photocatalysis, bulk calculations of band structures can still considerably reduce the combinatorial space of interest for experimental exploration.

Previous computational screening efforts to search for ternary metal oxides for overall water splitting revealed trends that enabled the rational targeting of photocatalytic performance by focusing on compounds containing particular elements and compositions.<sup>2–5</sup> Interestingly, compounds containing main-group elements comprised the majority of the active photocatalysts in a computational and experimental screening

Received: January 16, 2024 Revised: April 12, 2024 Accepted: April 30, 2024 Published: May 23, 2024





effort that considered more than 100 oxide materials.<sup>4</sup> These results were rationalized in terms of the high electron mobilities, and thus low carrier recombination rates, of these materials. Further screening efforts identified even more candidate photocatalysts that contained main-group elements.<sup>4</sup> These materials, which consisted of a *p*-block element along with an *s*-block (alkali or alkaline-earth) metal, exhibited band edges that were more electrochemically reducing than those of their binary *p*-block analogues and were thus more efficient in promoting hydrogen evolution for overall water splitting.

Ternary metal sulfide materials have also been found to be active photocatalysts for overall water splitting through similar data-driven discovery efforts.<sup>5</sup> In a recent study of mixed-metal oxides, oxysulfides, and sulfides, all of the computationally predicted sulfide targets were experimentally validated as being photocatalytically active for overall water splitting.<sup>5</sup> Often, metal sulfides have a more negative conduction band edge potential and a narrower band gap than their oxide counterparts, and these electronic-structure features lead to better absorption of visible wavelengths in the solar spectrum. These advantages, however, can be offset by the large effective mass of the photogenerated holes, as well as poor oxidative ability. Similar to the trends that emerged from computational screening of mixed-metal oxide materials, it is possible that the co-incorporation of s- and p-block elements into sulfide materials could help overcome these limitations. Indeed, recent reports have predicted s- and p-block ternary metal sulfides as active photocatalysts.  $^{7-10}$  However, as the chemical space of such materials is wide, broader screening efforts, coupled with experimental validation, will be important to effectively and efficiently explore candidate materials for photocatalytic water splitting.

To this end, we present a combined computational screening and experimental validation effort focused on mixed-metal sulfide compounds containing s- and p-block elements to identify potential photocatalysts for overall water splitting. We started by enumerating mixed-metal sulfide compounds from the Materials Project database<sup>11</sup> that contained both s- and p-block elements. Density functional theory calculations, improved for accuracy using Hubbard U corrections to self-interaction errors, were then applied to narrow the scope to eight candidate photocatalysts for overall water splitting, based on their band gaps and band alignments. From these eight materials, stability was assessed based on computational Pourbaix diagrams. Based on these criteria, four materials were then synthesized and evaluated for their photoresponsiveness, which is a prerequisite to demonstrating photocatalytic or photoelectrocatalytic activity. From this screening protocol, two compounds, MgIn<sub>2</sub>S<sub>4</sub> and BaSn<sub>2</sub>S<sub>5</sub>, were experimentally validated photoresponsive materials in potential ranges relevant for overall water splitting.

# METHODS

**Computational Methods.** In this study, we investigated a set of ternary sulfides containing alkali/alkaline earth metal cations (Li<sup>+</sup>, Na<sup>+</sup>, K<sup>+</sup>, Rb<sup>+</sup>, Cs<sup>+</sup>, Mg<sup>2+</sup>, Ca<sup>2+</sup>, Sr<sup>2+</sup>, Ba<sup>2+</sup>) with  $d^{10}$  closed-shell p-block metal cations (In<sup>3+</sup>, Sn<sup>4+</sup>, Sb<sup>5+</sup>, Bi<sup>5+</sup>, Ge<sup>4+</sup>, Ga<sup>3+</sup>) to direct our work toward photocatalytically active materials. The list of materials was screened from the *Materials Project* database<sup>11</sup> to ensure the materials have been synthesized and/or computationally predicted and have less than 50 atoms per unit cell to account for the computational resources required.

Electronic Structure Calculations. To predict band gaps and band edges, electronic structure calculations were performed using Quantum ESPRESSO. 12,13 The generalized-gradient approximation (GGA) to the exchange-correlation energy functional was employed, with the PBEsol parametrization, 14 and pseudopotentials from the SSSP library (PBEsol Precision v1.1.2). 15 Kinetic energy cutoffs of 60 Ry were used for the wave function and 480 for the charge density. The Brillouin zone was sampled using a Monkhorst—Pack k-point mesh with a spacing of 0.04 Å<sup>-1</sup>.

Hubbard U Correction and Spin-Orbit Coupling. All material structures were fully optimized at the GGA level prior to computing the Hubbard correction parameter. DFT + U calculations without spin-orbit coupling were conducted using the simplified formulation developed by Dudarev et al. 16 and Löwdin-orthogonalized orbitals were selected as Hubbard projectors. The Hubbard U parameters were applied to the 3p orbitals of sulfur and calculated using density-functional perturbation theory (DFPT).  $^{17}$  DFT + U calculations with spin-orbit coupling were conducted using the formulation developed by Liechtenstein et al.,  $^{18}$  with the Hubbard Uparameters determined without spin-orbit coupling. The PBEsol parametrization of GGA was used for spin-orbit coupling calculations, with fully relativistic norm-conserving pseudopotentials from the PseudoDojo library (ONCVPSP v0.4, with standard accuracy). 19,20 With norm-conserving pseudopotentials, a kinetic energy cutoff of 80 Ry was used for wave functions, with a corresponding cutoff of 320 Ry for the charge density.

Hybrid Functional Calculations. Hybrid functional calculations of band gaps were performed using the HSE06 functional.<sup>21</sup> Within the HSE06 framework, the exact exchange energy is partitioned into a short-range and a long-range part. 75% of the short-range part of the electron-electron interaction is estimated using the semilocal functional; the remaining 25% is computed as the Hartree-Fock exact exchange. The long-range part is calculated with the semilocal functional. For the semilocal functional, we used the PBEsol parametrization of the GGA, with scalar relativistic normconserving pseudopotentials from the PseudoDojo library (ONCVPSP v0.4, with standard accuracy). 19,20 Kohn-Sham wave functions and the exact-exchange term were both expanded on plane waves with a kinetic energy cutoff of 80 Ry. The Fock operator was sampled on a  $\Gamma$ -centered q-point mesh derived by coarsening the DFT k-point mesh by a factor of two in each direction of the reciprocal lattice. Finally, singularities of the Coulomb interaction in Fourier space were treated with the Gygi-Baldereschi scheme.<sup>22</sup>

**Screening Protocol.** The screening protocol consists of three steps. At the first step, band gaps  $E_{\rm g}$  of candidate photocatalysts are calculated at the DFT level of theory, and band edges are computed from band gaps as

$$E_{\rm VB} = E_{\rm FB} + E_{\rm g}/2e$$

$$E_{\rm CB} = E_{\rm FB} - E_{\rm g}/2e$$

where the flatband potential of the solid,  $E_{\rm FB}$ , is considered equal to the geometric mean  $\chi$  of the solid chemical elements' Mulliken electronegativities, divided by the elementary charge e:  $E_{\rm FB} = \chi/e$ . To account for typical errors in band gap predictions drawn from generalized-gradient DFT calculations, the selection criteria for water splitting, i.e. 1.5 eV <  $E_{\rm g}$  < 2.5 eV,  $E_{\rm VB}$  > 1.23 V vs SHE, and  $E_{\rm CB}$  < 0 V vs SHE, are modified.

Specifically, the domain defined by the standard selection criteria in the  $(E_{VB}, E_{CB})$  plane (see Figure S1) is transformed to include all points that satisfy: 1.5 eV <  $E_{\rm g}/\alpha$  < 2.5 eV, ( $E_{\rm VB}$  $-(1-\alpha) E_{FB})/\alpha > 1.23 \text{ V vs SHE, and } (E_{CB} - (1-\alpha) E_{FB})$  $/\alpha$  < 0 V vs SHE, for any  $\alpha$  ranging from 0.5 to 0.8 (corresponding to the typical underestimation factor of the band gap within GGA).<sup>3</sup> At the second step of the screening, band gaps of selected materials are calculated at the DFT + U level of theory. Then, standard selection criteria are applied, for band edges only:  $E_{VB} > 1.23 \text{ V}$  vs SHE, and  $E_{CB} < 0 \text{ V}$  vs SHE, with valence and conduction band edges calculated using DFT + U band gap estimations. Finally, the third step screens the pool of candidate photocatalysts for stability in water, by selecting only the materials with solid decomposition products at pH 7 and at a potential equal to the material flatband potential.

**Synthesis.** MgIn $_2$ S $_4$  was grown by a chemical vapor transport (CVT) method. Mg (32 mg, Sigma-Aldrich), In (300 mg, Sigma-Aldrich), and S (168 mg, Sigma-Aldrich) were placed at one end of a 16-in.-long quartz tube. The tube was sealed under vacuum and placed in a two-zone furnace. The hot end with the starting reagents was maintained at 950 °C, while the cold end was at 530 °C. This gradient was maintained for 2 weeks. This follows the preparation reported by Lee et al.  $^{2.5}$ 

 $Na_4Sn_3S_8$  was synthesized from  $Na_2S$  (111 mg, Sigma-Aldrich), SnS (342 mg, Alfa Aesar), and S (68 mg, Sigma-Aldrich). The powders were mixed in a glovebox and placed in a quartz tube. The tube was removed from the glovebox and quickly sealed under vacuum. The compound was heated in a box furnace to 680 °C for 1 week.

 $RbSbS_2$  was synthesized from Rb (85 mg, Sigma-Aldrich), Sb (122 mg, Sigma-Aldrich), and S (32 mg, Sigma-Aldrich) in a quartz tube under vacuum. The tube was heated in a box furnace to 500 °C for 5 h and allowed to cool ambiently to room temperature after this time.

 $BaSn_2S_5$  was synthesized following the procedure of Lui et al.  $^{26}$  BaS (158 mg, Alfa Aesar), Sn (222 mg, Sigma-Aldrich), and S (120 mg, Sigma-Aldrich) were ground together with an agate mortar and pestle. The sample was placed in an alumina crucible and sealed in a quartz tube under vacuum. The tube was then heated in a box furnace to 750 °C over 50 h and held at this temperature for 30 h. The furnace was cooled to 500 °C over 150 h, then to room temperature over 50 h.

**Characterization.** *Powder X-ray Diffraction.* Powder XRD data were collected on a Malvern Panalytical Empyrean diffractometer. The instrument was equipped with a copper source and operated at a voltage of 45 keV and a power of 40 kW. Powder XRD patterns were obtained using reflection mode and a PIXcel 3D detector.

Device Fabrication for Band Edge Determination. Each material was ground in a mortar and pestle to ensure fineness. Then, inks were made in concentrations of 0.004 mM material in ethanol, and these inks were sonicated for 1 h. 120  $\mu$ L of each ink was deposited on a 5 × 8 mm fluorine-doped tin oxide (FTO) slide, in 20  $\mu$ L increments, and these inks were annealed at 400 °C in a Thermolyne muffle furnace under an ambient atmosphere for 2 h. This temperature was chosen as it is below the synthesis temperature of all materials, which should maintain their stability.

Mott-Schottky Measurements. Mott-Schottky measurements were run on a Biologic SP-150 potentiostat using the Staircase Potentiometric EIS function, with data taken at 7

frequencies between 30 and 5 kHz. An initial scan was run from 1.5 to -1.5 V (E vs Ag/AgCl in saturated KCl), with subsequent scans for each material taken over a narrower range as determined by the location of the slope of the line. The electrolyte used was a pH 8 sodium phosphate buffer (Hydrion, 1g/100 mL), the reference electrode was Ag/AgCl in saturated KCl, and the counter electrode was a graphite rod. The working electrode was a device made from each material deposited on FTO, as previously described above for the band edge determination.

Chopped Illumination. Measurements were carried out on a Biologic SP-150 potentiostat using linear sweep voltammetry (LSV) at 5 mv/s, from 1.2 to -1.0 V (E vs Ag/AgCl in saturated KCl), and in pH 8 aqueous sodium phosphate buffer (approximately 1 g/100 mL). The reference electrode was Ag/AgCl in saturated KCl, and the counter electrode was a graphite rod, and the working electrode was the material on FTO. The samples were illuminated through a Starna cells quartz cuvette with a Newport Xenon 300 W lamp under the illumination of one sun. The chopping frequency was 0.2-0.3 Hz.

Flatband Potential. Two methods, Mott-Schottky and chopped illumination measurements, were used to determine the position of the flatband potential of the four synthesized materials. Mott-Schottky, while the most often used, is an indirect measurement of the flatband potential, whereas chopped illumination is a direct measurement. With these materials, only BaSn<sub>2</sub>S<sub>5</sub> showed a physically possible flatband potential by the Mott-Schottky method. As Mott-Schottky is a surface measurement, this could indicate that the other materials had surface defects that did not allow for adequate measurement of the flatband potential using this method. For BaSn<sub>2</sub>S<sub>5</sub>, Mott-Schottky was the method used to determine the flatband potential, and for the other three materials, which displayed clear transitions from anodic to cathodic photocurrent, chopped illumination was the best method of flatband potential determination.

Cyclic Voltammetry. Cyclic voltammetry measurements were performed on a Gamry Interface 1010E. The two stable materials, MgIn $_2$ S $_4$  and BaSn $_2$ S $_5$ , were sonicated with 20  $\mu$ L of Nafion perfluorinated resin (Sigma-Aldrich) in 400  $\mu$ L of water and 100  $\mu$ L isopropyl alcohol for 30 min. (Nafion was used to help with adhesion during multiple CV cycles). The catalyst inks were drop cast on fluorine-doped tin oxide (FTO) and cyclic voltammetry was performed under light and dark conditions. A graphite rod was used as the counter electrode and a Ag/AgCl (saturated KCl) reference electrode was utilized, as this electrode is stable under buffer conditions. The experiments were done in a phosphate buffer, at a pH of 8.

Diffuse Reflectance Spectroscopy. Diffuse reflectance UV–visible spectroscopy data were collected on a Shimadzu UV–visible spectrometer equipped with a Harrick Praying Mantis accessory. Tauc plots were calculated in order to determine the band gap of the material, with the ordinate plotted assuming a direct band gap  $(\gamma = 1/2)$ .

Gas Chromatography. Ten milligrams of sample was loaded into 20 mL of ultrapure (18  $M\Omega$ ) water in a sealed glass vessel. Samples were kept at ambient temperature in a water bath. Off-line gas chromatograms were collected by headspace injections onto an Agilent microGC, equipped with a molecular sieve column and thermal conductivity detector. Argon was used as the carrier gas. Illumination was provided by a 300 W Newport xenon lamp.

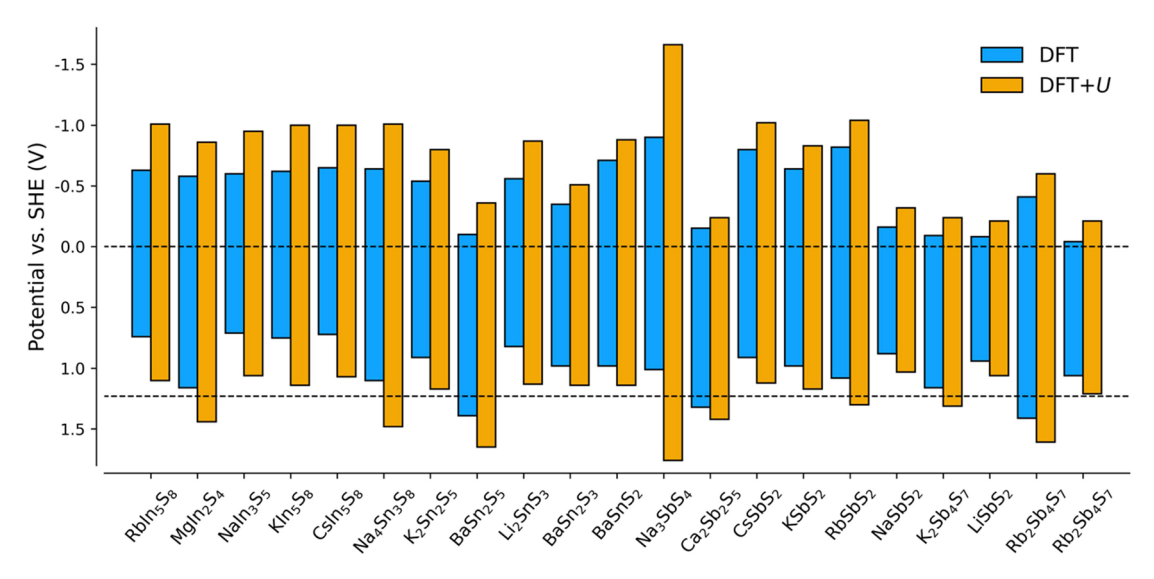


Figure 1. Band gaps and band edges calculated by DFT and DFT + U for the 21 materials that passed the first test of the screening protocol.

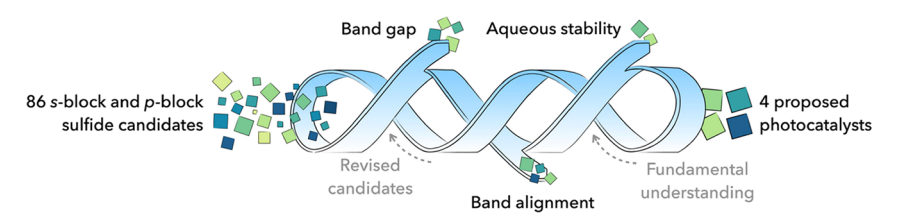


Figure 2. Representation of the data-driven screening process used to identify candidate photocatalysts. We began with 86 candidates, and screening based on band gap, band alignment, and aqueous stability resulted in four proposed photocatalysts, which were experimentally screened for photoresponsiveness. Each screening criterion decreased the number of candidate materials under consideration. Future efforts can further iterate between computation and experiment, expanding fundamental understanding and generating a revised list of candidates (as indicated with gray text and arrows).

# RESULTS AND DISCUSSION

Computational Predictions and Screening. Based on the design rationale detailed above, the computational screening of potential mixed-metal sulfide photocatalysts began with a pool of ternary-sulfide candidates containing an alkali or alkaline-earth metal (from the s-block) and a posttransition (semi)metal (from the p-block). Specifically, we focused on ternary metal sulfides containing the s-block metal cations Li<sup>+</sup>, Na<sup>+</sup>, K<sup>+</sup>, Rb<sup>+</sup>, Cs<sup>+</sup>, Mg<sup>2+</sup>, Ca<sup>2+</sup>, Sr<sup>2+</sup>, and Ba<sup>2+</sup> and the p-block metal cations In<sup>3+</sup>, Sn<sup>4+</sup>, Sb<sup>5+</sup>, Bi<sup>5+</sup>, Ge<sup>4+</sup>, and Ga<sup>3+</sup>. The resulting 86 candidate materials, listed in Table S1 of the Supporting Information, served as our initial parameter space. Further restrictions to limit the search space were imposed. We required that the materials have less than 50 atoms per unit cell so as to limit computational cost and that the materials have been demonstrated to be synthetically accessible in prior reports. For all 86 candidate photocatalysts, we calculated the band gaps and band edge energies using Hubbard-corrected density-functional theory (DFT + U). We applied Hubbard Uparameters to the 3p orbitals of sulfur and calculated their value self-consistently using density functional perturbation theory (Tables S1 and S2 and Figures 1 and S1). Based on these calculations, the candidate pool of 86 materials was narrowed to 21 that were computationally predicted to have appropriate band gaps and band edges (Figure 1 for visible light absorption. Out of these 21 materials, eight were anticipated to have band edge energies that would be appropriate for both the hydrogen evolution reaction (HER)

and oxygen evolution reaction (OER), as required for unassisted water splitting (Figure S2).

Next, we considered stability in aqueous environments by calculating Pourbaix diagrams (Figure S3, Table S3) for the eight candidate photocatalysts predicted to have appropriate band gaps and band alignments. For a candidate to be potentially stable under photocatalytic conditions, it should decompose into solids (as opposed to soluble ions), which may protect the photocatalyst against further corrosion, or have a low decomposition energy, corresponding to a small energy difference with respect to stable products. Previous accounts of instability under aqueous conditions, as in the case of  $Na_3SbS_4^{\ 28}$  and synthetic accessibility were also taken into consideration. Using these criteria (reached by the process shown in Figure 2), we selected four materials for synthesis and evaluation of photoresponsiveness under photocatalytically relevant conditions: MgIn<sub>2</sub>S<sub>4</sub>, BaSn<sub>2</sub>S<sub>5</sub>, RbSbS<sub>2</sub>, and Na<sub>4</sub>Sn<sub>3</sub>S<sub>8</sub>. These four materials were synthesized and tested as potential photo(electro)catalysts for overall water splitting.

**Synthesis and Testing.** The above materials were synthesized as bulk powders or single crystals, depending on available synthetic methods, using high-temperature solid-state reactions, as detailed in the Methods section. Briefly, MgIn<sub>2</sub>S<sub>4</sub> was synthesized by chemical vapor transport, <sup>25</sup> with a sealed evacuated quartz tube containing stoichiometric amounts of Mg, In, and S powders placed for 2 weeks in a two-zone furnace having one end at 950 °C and the other at 530 °C. Na<sub>4</sub>Sn<sub>3</sub>S<sub>8</sub> was synthesized by heating Na<sub>2</sub>S, SnS, and S at 680 °C for 1 week in a sealed evacuated quartz tube. RbSbS<sub>2</sub> was

synthesized by heating Rb, Sb, and S at 500 °C for 5 h in a sealed evacuated quartz tube.  $BaSn_2S_5$  was synthesized by heating a sealed evacuated quartz tube containing BaS, Sn, and S to 750 °C over 50 h and holding for 30 h, followed by cooling to 500 °C over 150 h, then to room temperature over 50 h. <sup>26</sup> Figure 3 shows powder X-ray diffraction (PXRD)

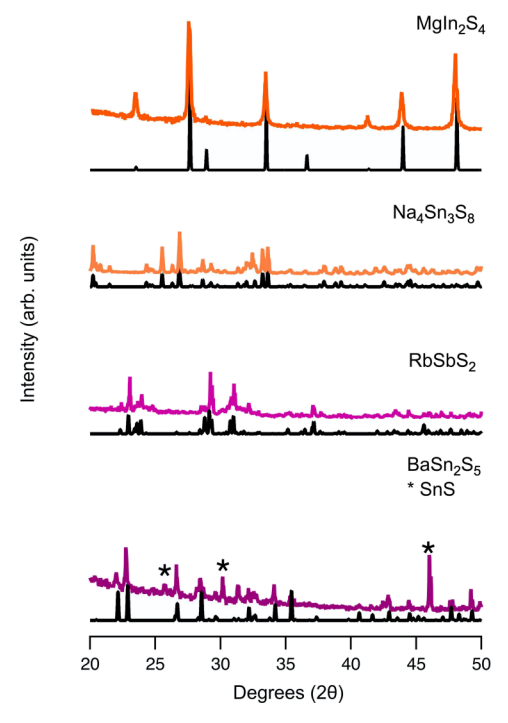


**Figure 3.** PXRD data for the four candidate photocatalysts. Experimental patterns are shown in various colors and the simulated patterns, based on crystallographic data from the Materials Project, are shown in black directly below each experimental pattern.

patterns for all four materials. Comparison of the experimental diffraction patterns with simulated patterns generated from crystallographic data available on the Materials Project<sup>11</sup> indicated that all reactions produced the targeted phases in high purity. The BaSn<sub>2</sub>S<sub>5</sub> sample contained a minor SnS impurity. For MgIn<sub>2</sub>S<sub>4</sub>, the material grew with a plate-like morphology oriented along the (422) plane. The simulated pattern, shown for comparison in Figure 2, includes 50% preferred orientation in this plane; additional comparisons are provided in Figure S4.

Tauc plots, derived from experimental UV—visible absorption spectra, are shown in Figure S5, and a comparison of the experimental band gaps and the computationally determined band gaps are presented in Figure 3. The experimentally determined band gap for  $MgIn_2S_4$  was 1.81 eV, which matches

favorably with a previous experimental report of 1.98 eV.<sup>29</sup> BaSn<sub>2</sub>S<sub>5</sub> has a literature band gap of 2.35 eV, which is consistent with our experimentally measured band gap (2.1 eV).26 To our knowledge, the band gaps for Na<sub>4</sub>Sn<sub>3</sub>S<sub>8</sub> and RbSbS<sub>2</sub> have not previously been reported. We measured band gaps of 1.61 and 1.55 eV for Na<sub>4</sub>Sn<sub>3</sub>S<sub>8</sub> and RbSbS<sub>2</sub>, respectively. These materials each possessed only one major transition in the visible region, giving reasonable confidence that these transitions correspond to optical band gaps of the materials. Unexpectedly, we found that DFT calculations without self-interaction correction were in better agreement with the experimental results than self-interaction-corrected DFT + U predictions for all materials except BaSn<sub>2</sub>S<sub>5</sub> (Figure 3 and Table 1). To critically validate the accuracy of DFT + Upredictions, we calculated band gaps with spin-orbit coupling but found a maximum spin-orbit deviation of only -0.04 eV, for RbSbS<sub>2</sub> (Table S2). Although our calculations also neglected thermal vibrations and excitonic contributions, these effects are not expected to affect band gaps by more than  $\sim\!0.4$  eV,  $^{30}$  and hence cannot explain the difference between DFT + U and experimental results. Finally, to test the Hubbard *U* correction of self-interaction errors, we carried out calculations using the HSE06 range-separated hybrid functional (Figure 4 and Table 1). Hybrid functionals, while more

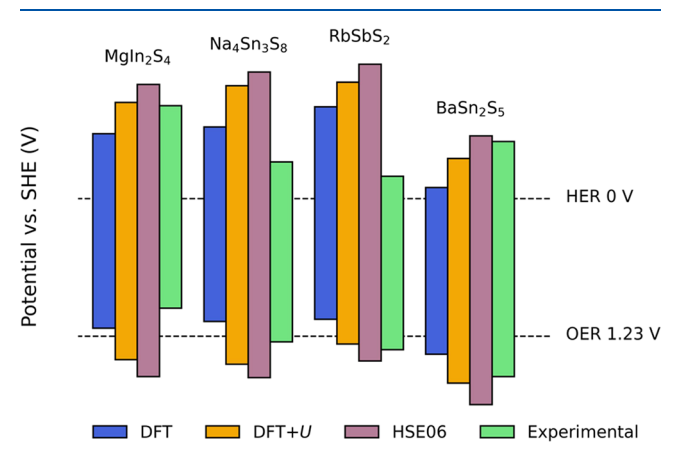


**Figure 4.** Experimental band gaps determined from Tauc plots and band edges determined from chopped illumination (CI) flatband regions, compared to band gaps and band edges calculated by DFT, DFT + *U*, and HSE06 methods.

computationally expensive, are potentially more accurate than DFT + U band gap calculations and have been successfully applied to sulfide materials previously. <sup>31–33</sup> In line with DFT + U, HSE06 estimates are systematically larger than experimental measurements. The residual discrepancies between theory and experiment might come from high concentrations of sulfur vacancies. Sulfur vacancies are common in sulfide materials,

Table 1. Band Gaps  $(E_g)$  and Band Edge Potentials  $(E_{CB}$  for Conduction Bands and  $E_{VB}$  for Valence Bands) Computed from DFT, DFT +  $U_r$  and HSE06, Compared with Experimental Measurements

	DFT			DFT + $U$			HSE06			experimental		
	(eV)	$E_{\mathrm{VB}}$ (V vs SHE)	$E_{\rm CB}~({ m V}~{ m vs}~{ m SHE})$	(eV)	$E_{\mathrm{VB}}$ (V vs SHE)	$E_{\mathrm{CB}}$ (V vs SHE)	(eV)	$E_{ m VB}~({ m V~vs}~{ m SHE})$	$E_{\rm CB}$ (V vs SHE)	$E_{\rm g}({ m eV})$	$E_{ m VB}~({ m V~vs}~{ m SHE})$	$E_{\rm CB}~({ m V}~{ m vs}~{ m SHE})$
$MgIn_2S_4$	1.74	1.16	-0.58	2.30	1.44	-0.86	2.61	1.59	-1.02	1.81	0.98	-0.83
$Na_4Sn_3S_8$	1.74	1.10	-0.64	2.49	1.48	-1.01	2.73	1.60	-1.13	1.61	1.28	-0.33
$RbSbS_2$	1.90	1.08	-0.82	2.34	1.30	-1.04	2.65	1.45	-1.20	1.55	1.35	-0.2
$BaSn_2S_5$	1.49	1.39	-0.10	2.01	1.65	-0.36	2.40	1.84	-0.56	2.1	1.59	-0.51

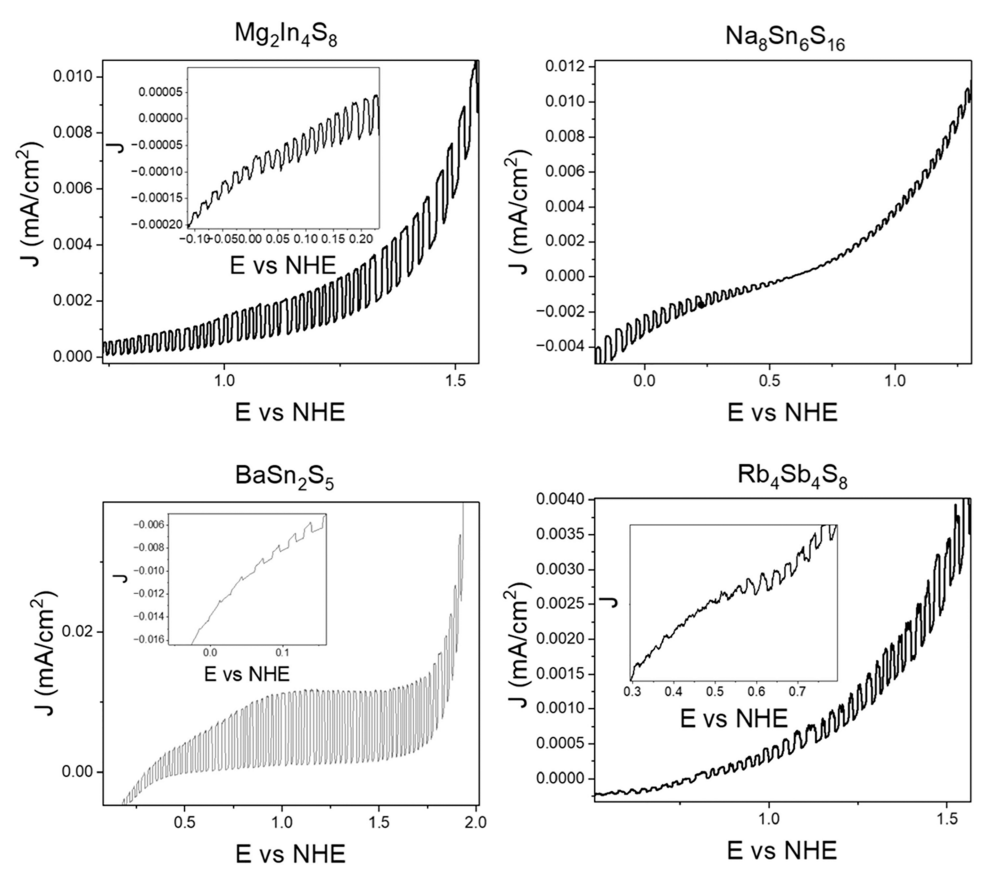


Figure 5. Band edge determination and photocurrent response from chopped illumination experiments.

given the volatility of sulfur and the high temperatures at which the sulfide powders are prepared. These sulfur vacancies are not accounted for in computational predictions and could narrow the band gaps of sulfide compounds due to the formation of trap states.<sup>34</sup> Current computational methods are not yet able to systematically capture the effects of such trap states at a reasonable computational cost. Furthermore, there may be additional material modifications, such as the formation of secondary phases (along with interfaces) under catalytic conditions that could further modify properties. Such modeling of active phases represents an exciting frontier for future research efforts. Based on these results and considerations, a theoretical and experimental understanding of vacancies and their effect on the band gaps will be essential for future photocatalysis discovery efforts in such systems.

All four experimentally tested materials absorb light in the range of 1-3 eV, which includes the visible region. Furthermore, chopped illumination results offer evidence that all four materials exhibit a photoinduced current (Figure 5). MgIn<sub>2</sub>S<sub>4</sub> and BaSn<sub>2</sub>S<sub>5</sub> exhibited the largest change in current under illumination. This result is important, as it indicates that illumination excites mobile carriers, which are able to travel to the surface and facilitate catalysis. Despite some deviations between the calculated and experimental band edge positions, three of the predicted materials still had an energy that overlapped with the relevant potentials for overall water splitting, with MgIn<sub>2</sub>S<sub>4</sub> being the only material that did not overlap with the OER potential. Under an applied potential, as described later, MgIn<sub>2</sub>S<sub>4</sub> still exhibited a photoenhanced current at OER potentials, but this lack of overlap still is

kinetically unfavorable to the OER and may inhibit photocatalysis without an applied electrochemical bias.

Potential photocatalytic performance for overall water splitting can be evaluated from band alignment and redox stability. In an initial test of stability in water under illumination, Na<sub>4</sub>Sn<sub>3</sub>S<sub>8</sub> and RbSbS<sub>2</sub> were not stable when illuminated for 24 h under photocatalytically relevant conditions (with no applied voltage and at pH 7 to be compatible with a phosphate buffer) and thus were not further explored for activity. This instability is evident in Figure S6, where PXRD data for each of the materials as-synthesized and after catalysis are shown. Reference patterns for decomposition products, as simulated from structures reported in the literature, are shown in blue. 35-37 Excluding BaSn<sub>2</sub>S<sub>5</sub>, whose decomposition energy is found to be highly sensitive to the estimated flatband potential, the two unstable materials had the largest decomposition energy (calculated at the experimental flatband potential), and so would be expected to be most susceptible to degradation (Table S4). Na<sub>4</sub>Sn<sub>3</sub>S<sub>8</sub> decomposed to sulfur and SnO2. While SnO2 was a predicted decomposition product, sulfur, rather than the predicted aqueous sulfate ion, formed. RbSbS2 decomposed into Sb2O3 rather than HSbO<sub>2</sub>, or the predicted Rb<sub>2</sub>Sb<sub>4</sub>O<sub>11</sub> solid. This comparison of theoretical and experimental (in)stability indicates that key aspects of decomposition behavior were captured, but some different products other than those expected, formed. MgIn<sub>2</sub>S<sub>4</sub> and BaSn<sub>2</sub>S<sub>5</sub> exhibited moderate stability, without observable formation of crystalline decomposition products. There were minor impurity peaks that arose in MgIn<sub>2</sub>S<sub>4</sub>. While these peaks could not be indexed to a known phase, due to the small number of peaks, it can be

hypothesized that binary sulfides or oxides may have formed. These phases may form a passivating layer on the surface that inhibits further decomposition, considering that gross degradation was not observed. However, long-term stability studies, which are beyond the scope of this study, would be required to determine if such degradation would proceed over time.  $BaSn_2S_5$  decreased in crystallinity, with PXRD data demonstrating peak broadening and loss of peak intensity. However, the ternary  $BaSn_2S_5$  phase remained, with no binary crystalline oxides or sulfides observable by PXRD.

Despite exhibiting moderate phase stability under photocatalytic conditions, BaSn<sub>2</sub>S<sub>5</sub> and MgIn<sub>2</sub>S<sub>4</sub> did not generate hydrogen under 24 h of illumination, as assessed by gas chromatography. For MgIn<sub>2</sub>S<sub>4</sub>, activity for overall water splitting could be hampered by the lack of overlap of the valence band edge with the OER potential. This would lead to an energetic inhibition of the oxidization of water, where holes are at too high of energy and thus unable to generate O<sub>2</sub>. However, BaSn<sub>2</sub>S<sub>5</sub>, which has overlapping potentials for overall water splitting, was also inactive. This behavior may be attributable to surface inhibition of the binding and release of intermediates, which future studies can interrogate in greater detail. A different oxidation reaction could also be chosen. To this end, we screened ethanol, methanol, and isopropyl alcohol as possible sacrificial reductants, yet did not observe hydrogen by gas chromatography. While outside the scope of overall water-splitting catalysis, there are other possibilities for alternative oxidation reactions, such as the use of hydroquinone.38

To further investigate the photoresponsiveness of these materials, cyclic voltammetry was applied. By comparing the current in the dark and under illumination, the presence of photoenhanced current and photoelectrocatalytic activity could be assessed. The electrodes were prepared by dropcasting a catalyst ink on FTO glass. Experiments were first run in the dark, cycling five times between potentials relevant to the HER and the OER. This procedure was observed to be sufficient to lead to steady performance cycle to cycle. Five cycles were then run under illumination. This process was repeated three times to ensure reproducibility and not activation or deactivation over time. For both MgIn<sub>2</sub>S<sub>4</sub> and BaSn<sub>2</sub>S<sub>5</sub>, a photoenhancement of current was observed at the HER and the OER potentials (Figure 6). This observation indicates that MgIn<sub>2</sub>S<sub>4</sub> and BaSn<sub>2</sub>S<sub>5</sub> could perform as photoabsorbers for bifunctional electrodes. While the current for the photoelectrochemical overall water splitting reaction is insufficient to allow these materials to efficiently catalyze water splitting, the increase in photocurrent is significant for demonstrating their photoelectrochemical activity, which is an important step in the data-intensive identification of new water splitting photocatalysts. Current could be lost due to defects, creating trap states.<sup>39</sup> If this is the case, synthesis techniques that minimize defects could improve the performance of these materials as photoelectrodes. These discovered materials could also be active for water splitting with a cocatalyst, as in a Z-scheme photocatalyst construct.

# CONCLUSIONS

In conclusion, we report a combined computational and experimental investigation focused on screening main-group metal sulfides for photoelectrochemical responsiveness, as a first step toward more comprehensively evaluating photocatalytic activity. The computational screening workflow

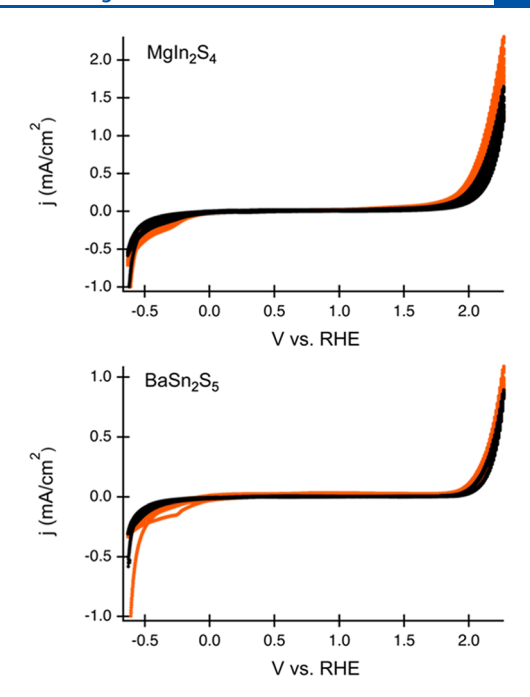


**Figure 6.** Cyclic voltammetry data for the catalyst materials under illumination (orange) and in the dark (black). The potentials are calculated based on the reversible hydrogen electrode (RHE), adjusting for the solution pH.

narrowed a pool of 86 candidates to four, which were experimentally interrogated. Two were found to be photoelectrochemically active, which was the goal of the screening effort. The two photoelectro-active materials identified in this work offer evidence that further study of this promising class of materials is warranted. Specifically, with this data-driven approach, we have revealed electronic trends that allow band gap tuning toward photoelectrocatalytic overall water splitting. We then experimentally investigated these materials, allowing rigorous evaluation of theoretical methods for fundamental material property predictions, such as electronic structure, and predictions relevant to operando performance, such as band edge alignment and stability. This comparative evaluation underscores the need to account for midgap states related to defects such as sulfur vacancies, which may reduce the band gaps of sulfide materials. In the future, the validity of band gap calculations can be supported through advanced highthroughput synthesis techniques, such as thin film growth, where such vacancies can be controlled or largely eliminated. 40 However, it is likely such vacancies would still arise operando, motivating computational modeling of the active catalyst. Overall, this work demonstrates that sulfides consisting of a pblock element along with an s-block metal, are a promising phase space for identifying photoelectrodes and catalysts for overall water splitting. Furthermore, the discovery of such materials can be greatly accelerated by computational, datadriven approaches.

# ASSOCIATED CONTENT

# Supporting Information

The Supporting Information is available free of charge at https://pubs.acs.org/doi/10.1021/acs.jpcc.4c00341.

Data of the calculated band gaps and stabilities, additional experimental details, and analysis of PXRD and optical data (PDF)

#### AUTHOR INFORMATION

### **Corresponding Authors**

Héctor D. Abruña — Department of Chemistry, Cornell University, Cornell, New York 14850, United States; orcid.org/0000-0002-3948-356X; Email: hda1@cornell.edu

Ismaila Dabo — Depatment of Materials Science and Engineering, The Pennsylvania State University, University Park, Pennsylvania 16802, United States; Department of Physics and Materials Research Institute, The Pennsylvania State University, University Park, Pennsylvania 16802, United States; orcid.org/0000-0003-0742-030X; Email: dabo@psu.edu

Raymond E. Schaak – Department of Chemistry, Materials Research Institute, and Department of Chemical Engineering, The Pennsylvania State University, University Park, Pennsylvania 16802, United States; orcid.org/0000-0002-7468-8181; Email: res20@psu.edu

#### **Authors**

Rowan R. Katzbaer – Department of Chemistry, The Pennsylvania State University, University Park, Pennsylvania 16802, United States; orcid.org/0000-0002-6028-2359

Simon Gelin – Depatment of Materials Science and Engineering, The Pennsylvania State University, University Park, Pennsylvania 16802, United States

Monica J. Theibault – Department of Chemistry, Cornell University, Cornell, New York 14850, United States

Mohammed M. Khan – Department of Materials Science and Engineering, The Pennsylvania State University, University Park, Pennsylvania 16802, United States

Cierra Chandler – Depatment of Materials Science and Engineering, The Pennsylvania State University, University Park, Pennsylvania 16802, United States

Nicola Colonna – Laboratory for Materials Simulations, Paul Scherrer Institute, 5232 Villigen, Switzerland; National Centre for Computational Design and Discovery of Novel Materials (MARVEL), École Polytechnique Fédérale de Lausanne, 1015 Lausanne, Switzerland; orcid.org/0000-0002-6106-6316

Zhiqiang Mao — Department of Chemistry and Department of Physics, The Pennsylvania State University, University Park, Pennsylvania 16802, United States; orcid.org/0000-0002-4920-3293

Complete contact information is available at: https://pubs.acs.org/10.1021/acs.jpcc.4c00341

#### **Author Contributions**

The synthesis, optical band gap determination, and photo-electrochemical activity experiments were performed by R.R.K. under the supervision of R.E.S. and Z.Q.M. M.J.T. performed the electrochemical band edge determination under the supervision of H.D.A. The initial band structure and band gap computations (DFT and DFT + U without spin—orbit coupling) were performed by C.C. and M.M.K.; the refined band structure calculations (HSE, DFT + U with spin—orbit coupling) were performed by S.G. and N.C. Band alignment and stability analyses were carried out by S.G. and M.M.K. Computational screening criteria were developed by S.G. and M.M.K. I.D. supervised the computational work. All authors contributed to writing the manuscript.

#### Notes

The authors declare no competing financial interest.

# ACKNOWLEDGMENTS

This work was primarily supported by the National Science Foundation through the Penn State Materials Research Science and Engineering Center (MRSEC), grant number DMR-2011839. XRD and UV—visible data were obtained at the Penn State Materials Research Institute. M.M.K. and I.D. acknowledge partial support from the DMREF and INFEWS programs of the National Science Foundation under Grant No. DMREF-1729338. N.C. acknowledges support from the Swiss National Science Foundation (SNSF) through its National Centre of Competence in Research (NCCR) MARVEL. Calculations were performed on the Roar supercomputer of the Institute for Computational and Data Sciences (ICDS) at the Pennsylvania State University.

# REFERENCES

- (1) Tee, S. Y.; Win, K. Y.; Teo, W. S.; Koh, L. D.; Liu, S.; Teng, C. P.; Han, M. Y. Recent Progress in Energy-Driven Water Splitting. *Adv. Sci.* **2017**, *4* (5), 1600337.
- (2) Wu, Y.; Lazic, P.; Hautier, G.; Persson, K.; Ceder, G. First Principles High Throughput Screening of Oxynitrides for Water-Splitting Photocatalysts. *Energy Environ. Sci.* **2013**, 6 (1), 157–168.
- (3) Xiong, Y.; Campbell, Q. T.; Fanghanel, J.; Badding, C. K.; Wang, H.; Kirchner-Hall, N. E.; Theibault, M. J.; Timrov, I.; Mondschein, J. S.; Seth, K.; et al. Optimizing Accuracy and Efficacy in Data-Driven Materials Discovery for the Solar Production of Hydrogen. *Energy Environ. Sci.* **2021**, *14* (4), 2335–2348.
- (4) Gelin, S.; Kirchner-Hall, N. E.; Katzbaer, R. R.; Theibault, M. J.; Xiong, Y.; Zhao, W.; Kahn, M. M.; Andrewlavage, E.; Orbe, P.; Baksa, S. M.; et al. Ternary Oxides of *s* and *p*-Block Metals for Photocatalytic Solar-to-Hydrogen Conversion. *PRX Energy* **2024**, *3*, No. 013007.
- (5) Katzbaer, R. R.; Theibault, M. J.; Kirchner-Hall, N. E.; Mao, Z.; Dabo, I.; Abruña, H. D.; Schaak, R. E. Understanding the Photoelectrochemical Properties of Theoretically Predicted Water-Splitting Catalysts for Effective Materials Discovery. *Adv. Energy Mater.* **2022**, *12* (46), 2201869.
- (6) Di, T.; Xu, Q.; Ho, W.; Tang, H.; Xiang, Q.; Yu, J. Review on Metal Sulphide-based Z-scheme Photocatalysts. *ChemCatChem.* **2019**, *11* (5), 1394–1411.
- (7) Guo, P.; Xiao, Y.; Mo, R.; Li, X.; Li, H. Coherent-Twinning-Enhanced Solar Water Splitting in Thin-Film Cu<sub>2</sub>ZnSnS<sub>4</sub> Photocathodes. *ACS Energy Lett.* **2023**, *8* (1), 494–501.
- (8) Hajiahmadi, Z.; Naghavi, S. S. Sn(IV) Polyanionic Materials as Efficient Visible-Light-Driven Water-Splitting Photocatalysts. *J. Phys. Chem. C* **2022**, *126* (50), 21243–21252.
- (9) McKeever, H.; Patil, N. N.; Palabathuni, M.; Singh, S. Fuctional Alkali Metal-Based Ternary Chalcogenides: Design, Properties, and Opportunities. *Chem. Mater.* **2023**, *35*, 9833.
- (10) Shen, C.; Li, T.; Zhang, Y.; Xie, R.; Long, T.; Fortunato, N. M.; Liang, F.; Dai, M.; Shen, J.; Wolverton, C. M.; et al. Accelerated Screening of Ternary Chalcogenides for Potential Photovoltaic Applications. J. Am. Chem. Soc. 2023, 145, 21925–21936.
- (11) Jain, A.; Ong, S. P.; Hautier, G.; Chen, W.; Richards, W. D.; Dacek, S.; Cholia, S.; Gunter, D.; Skinner, D.; Ceder, G.; et al. Commentary: The materials project: A materials genome approach to accelerating materials innovation. *APL Materials* **2013**, *1* (1), No. 011002.
- (12) Giannozzi, P.; Baroni, S.; Bonini, N.; Calandra, M.; Car, R.; Cavazzoni, C.; Ceresoli, D.; Chiarotti, G. L.; Cococcioni, M.; Dabo, I.; et al. QUANTUM ESPRESSO: a modular and open-source software project for quantum simulations of materials. *J. Phys.: Condens. Matter* **2009**, *21*, No. 395502.

- (13) Giannozzi, P.; Andreussi, O.; Brumme, T.; Bunau, O.; Bardelli, M. B.; Calandra, M.; Car, R.; Cavazzoni, C.; Ceresoli, D.; Cococcioni, M.; et al. Advanced capabilities for materials modelling with Quantum ESPRESSO. *J. Phys.: Condens. Matter* **2017**, *29*, No. 465901.
- (14) Perdew, J. P.; Ruzsinszky, A.; Csonka, G. I.; Vydrov, O. A.; Scuseria, G. E.; Constantin, L. A.; Zhou, X.; Burke, K. Restoring the Density-Gradient Expansion for Exchange in Solids and Surfaces. *Phys. Rev. Lett.* **2008**, *100*, No. 136406.
- (15) Prandini, G.; Marrazzo, A.; Castelli, I. E.; Mounet, N.; Marzari, N. Precision and efficiency in solid-state pseudopotential calculations. *npj Comput. Mater.* **2018**, *4*, 72.
- (16) Dudarev, S. L.; Botton, G. A.; Savraso, S. Y.; Humphreys, C. J.; Sutton, A. P. Electronenergy-loss spectra and the structural stability of nickel oxide: An LSDA+U study. *Phys. Rev. B* **1998**, *57*, 1505.
- (17) Timrov, I.; Marzari, N.; Cococcioni, M. HP a code for the calculation of Hubbard parameters using density-functional perturbation theory. *Comput. Phys. Commun.* **2022**, 279, No. 108455.
- (18) Liechtenstein, A. I.; Anisimov, V. I.; Zaanen, J. Density-functional theory and strong interactions: Orbital ordering in Mott-Hubbard insulators. *Phys. Rev. B* **1995**, *52*, No. R5467(R).
- (19) van Setten, M. J.; Giantomassi, M.; Bousquest, E.; Verstraete, M. J.; Hamann, D. R.; Gonze, X.; Rignanese, G.-M. The PseudoDojo: Training and grading a 85 element optimized norm-conserving pseudopotential table. *Comput. Phys. Commun.* **2018**, 226, 39–54.
- (20) Hamann, D. R. Optimized norm-conserving Vanderbilt pseudopotentials. *Phys. Rev. B* **2013**, *88*, No. 085117.
- (21) Heyd, J.; Scuseria, G. E.; Ernzerhof, M. Hybrid functionals based on a screened coulomb potential. *J. Chem. Phys.* **2003**, *118*, 8207.
- (22) Gygi, F.; Baldereschi, A. Self-consistent Hartree-Fock and screened-exchange calculations in solids: Application to silicon. *Phys. Rev. B* **1986**, *34*, No. 4405(R).
- (23) Butler, J. M. A.; Ginley, D. S. Prediction of flatband potentials at semiconductor-electrolyte interfaces from atomic electronegativities. *J. Electrochem. Soc.* 1978, 125, 228.
- (24) Xu, Y.; Schoonen, M. A. The absolute energy positions of conduction and valence bands of selected semiconducting minerals. *Am. Mineral.* **2000**, *85*, 543.
- (25) Lee, S. J.; Kim, J. E.; Park, H. Y. Optical Absorption of Co<sup>2+</sup> in MgIn<sub>2</sub>S<sub>4</sub>, CdIn<sub>2</sub>S<sub>4</sub>, and HgIn<sub>2</sub>S<sub>4</sub> Spinel Crystals. *J. Mater. Res.* **2003**, 18 (3), 733–736.
- (26) Luo, Z. Z.; Lin, C. S.; Cheng, W. D.; Zhang, H.; Zhang, W. L.; He, Z. Z. Syntheses, Characterization, and Optical Properties of Ternary Ba–Sn–S System Compounds: Acentric Ba<sub>7</sub>Sn<sub>5</sub>S<sub>15</sub>, Centric BaSn<sub>2</sub>S<sub>5</sub>, and Centric Ba<sub>6</sub>Sn<sub>7</sub>S<sub>20</sub>. *Inorg. Chem.* **2013**, 52 (1), 273–279.
- (27) Makula, P.; Michal, P.; Macyk, W. How to Correctly Determine the Band Gap Energy of Modified Semiconductor Photocatalysts Based on UV-Vis Spectra. *J. Phys. Chem. Lett.* **2018**, 9 (23), 6814–6817.
- (28) Banerjee, A.; Park, K. H.; Heo, J. W.; Nam, Y. J.; Moon, C. K.; Oh, S. M.; Hong, S.-T.; Jung, Y. S. Na<sub>3</sub>SbS<sub>4</sub>: A solution Processable Sodium Superionic Conductor for All-Solid-State Sodium-Ion Batteries. *Angew. Chem., Int. Ed.* **2016**, *55*, 9634.
- (29) Chen, W.; Hua, Y.-X.; Wang, Y.; Huang, T.; Liu, T.-Y.; Liu, X.-H. Two-Dimensional Mesoporous g- $C_3N_4$  Nanosheet-Supported MgIn<sub>2</sub>S<sub>4</sub> Nanoplates as Visible-Light-Active Heterostructures for Enhanced Photocatalytic Activity. *J. Catal.* **2017**, 349, 8–18.
- (30) Wang, H.; Tal, A.; Bischoff, T.; Gono, P.; Pasquarello, A. Accurate and efficient band-gap predictions for metal halide perovskites at finite temperature. *npj Comput. Mater.* **2022**, *8*, 237.
- (31) Chen, B. W. J.; Xu, L.; Mavrikakis, M. Computational Methods in Heterogeneous Catalysis. *Chem. Rev.* **2023**, *121* (2), 1007–1048.
- (32) Liu, Y.; Song, X.-D.; Zhang, R.-C.; Zhou, F.-Y.; Zhang, J.-W.; Jaing, X.-M.; Ji, M.; An, Y.-L. Solvothermal Syntheses and Characterizations of Four Quaternary Copper Sulfides  $BaCu_3MS_4$  (M = In, Ga) and  $BaCu_2MS_4$  (M = Sn, Ge). *Inorg. Chem.* **2019**, 58 (22), 15101–15109.
- (33) Sujith, C. P.; Mathew, T.; Mathew, V. Density Functional Study of Electronic and Optical Properties of Quasi-One-Dimensional Metal

- Tin Sulfides  $MSnS_3$  (M = Hf, Zr). Solid State Sci. 2021, 116, No. 106608.
- (34) Zhang, N.; Xing, Z.; Li, Z.; Zhou, W. Sulfur vacancy engineering of metal sulfide photocatalysts for solar energy conversion. *Chem. Catalysis* **2023**, 3 (1), No. 100375.
- (35) Rettig, S. J.; Trotter, J. Refinement of the Structure of Orthorhombic Sulfur,  $\alpha$ -S<sub>8</sub>. Acta Crystallogr. Sect. C Cryst. Struct. Commun. 1987, 43 (12), 2260–2262.
- (36) Svensson, C. Refinement of the Crystal Structure of Cubic Antimony Trioxide, Sb<sub>2</sub>O<sub>3</sub>. Acta Crystallogr. Sect. B Struct. Crystallogr. Cryst. Chem. 1975, 31 (8), 2016–2018.
- (37) Baur, W. H.; Khan, A. A. Rutile-Type Compounds IV. SiO<sub>2</sub>, GeO<sub>2</sub> and a Comparison with Other Rutile-Type Structures. *Acta Crystallogr. Sect. B Struct. Crystallogr. Cryst. Chem.* **1971**, 27 (11), 2133–2139.
- (38) Lapides, A. M.; Sherman, B. D.; Brennaman, M. K.; Dares, C. J.; Skinner, K. R.; Templeton, J. L.; Meyer, T. J. Synthesis, Characterization, and Water Oxidation by a Molecular Chromophore-Catalyst Assembly Prepared by Atomic Layer Deposition. The "Mummy" Strategy. *Chemical Science* **2015**, *6*, 6398–6406.
- (39) Zafar, Z.; Yi, S.; Li, J.; Chuanqi, Li; Zhu, Y.; Zada, A.; Yao, W.; Liu, Z. Recent Development in Defects Engineered Photocatalysts: An Overview of the Experimental and Theoretical Strategies. *Energy Environ. Mater.* **2022**, *5*, 68–144.
- (40) Zakutayev, A.; Wunder, N.; Schwarting, M.; Perkins, J. D.; White, R.; Munch, K.; Tumas, W.; Phillips, C. An open experimental database for exploring inorganic materials. *Sci. Data* **2018**, *5*, No. 180053.